Full-waveform inversion at Santorini volcano

Kajetan Chrapkiewicz, Michele Paulatto, Joanna Morgan, Mike Warner, Benjamin Heath, Emilie Hooft, Brennah McVey, Douglas Toomey, Paraskevi Nomikou, and Constantinos Papazachos

EGU2020 "Sharing Geoscience Online", 8 May 2020

About

- this presentation in other formats (Jupyter notebook, HTML) will be available at: https://github.com/kmch/EGU2020-19836 (https://github.com/kmch/EGU2020-19836)
- repository with the Python package used as a framework of this study: https://github.com/kmch/FullwavePy/ (https://github.com/kmch/FullwavePy/)
- my email: k.chrapkiewicz17@imperial.ac.uk and personal webpage: http://www.imperial.ac.uk/people/k.chrapkiewicz17 (http://www.imperial.ac.uk/people/k.chrapkiewicz17); don't hesitate to contact me with any questions.

Santorini geology (Kilias et al. 2013)

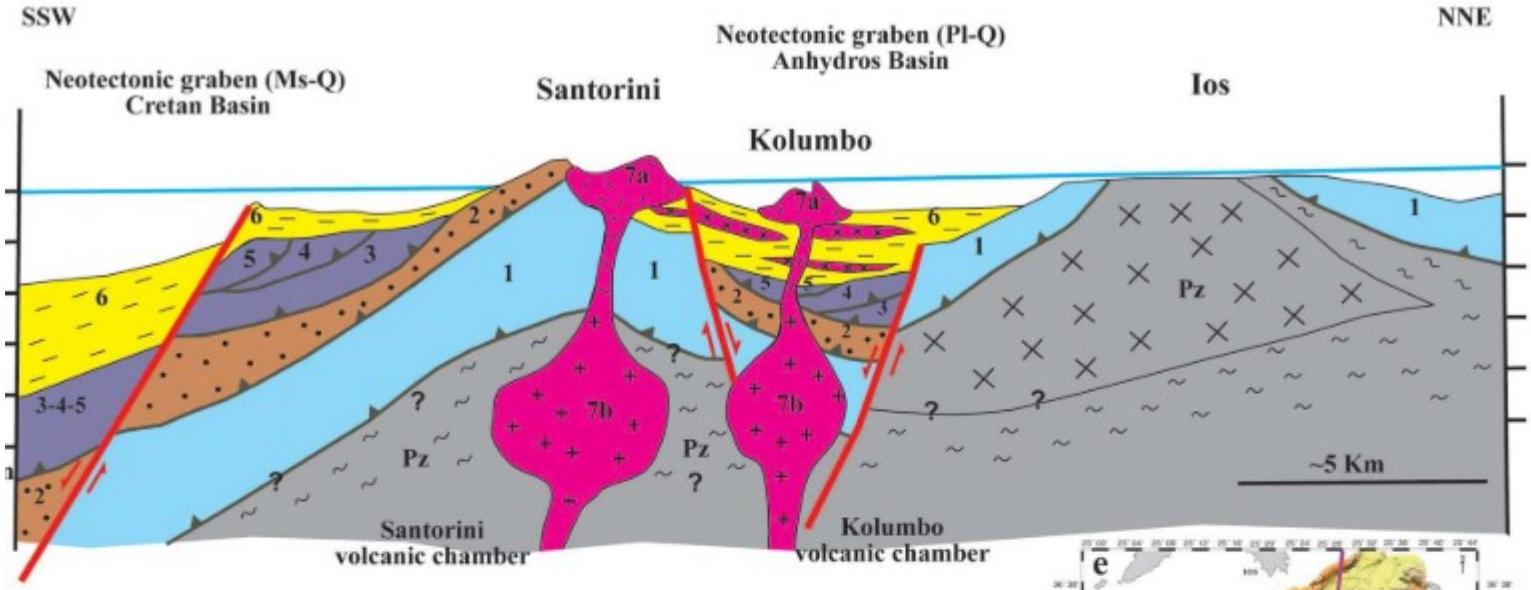

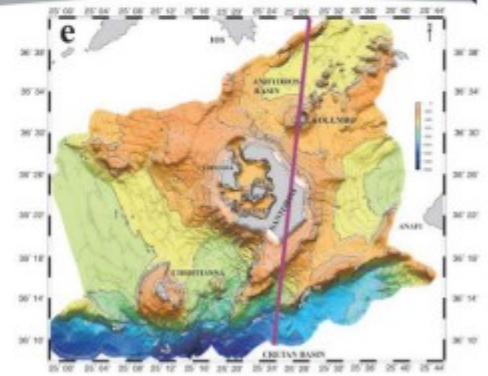

Legend

Post-Alpine

7a: Volcanic rocks
7b: Magmatic chambers

Pl-Q: Plio(?)-Quaternary sediments with volcanic intercalations
Ms-Q: Late Miocene-Quaternary sediments (molasse)

Alpine

Anafi Late Cretaceous allochthon metamorphic units (greenschists and granites)

Non metamorphic Mesozoic carbonates and Tertiary flysch of Proph. Ilias (Santorini) / Anafi autochthon

Athinios (Santorini)/Ios Tertiary metamorphics (blueschists)

Pre-Alpine

Paleozoic Metamorphic Basement including Carboniferous granites (ortho-gneisses)

Geological boundary

Alpine tectonic contacts (thrusts and extensional detachments)

Neotectonic fault zone

PROTEUS experiment

A 3D wide-angle, multi-azimuth seismic dataset from the recent PROTEUS experiment (Hooft et al. 2017) acquired with ca. 150 ocean-bottom/land seismic stations and ca. 14,000 air-gun shots.

Figure by M. Paulatto.

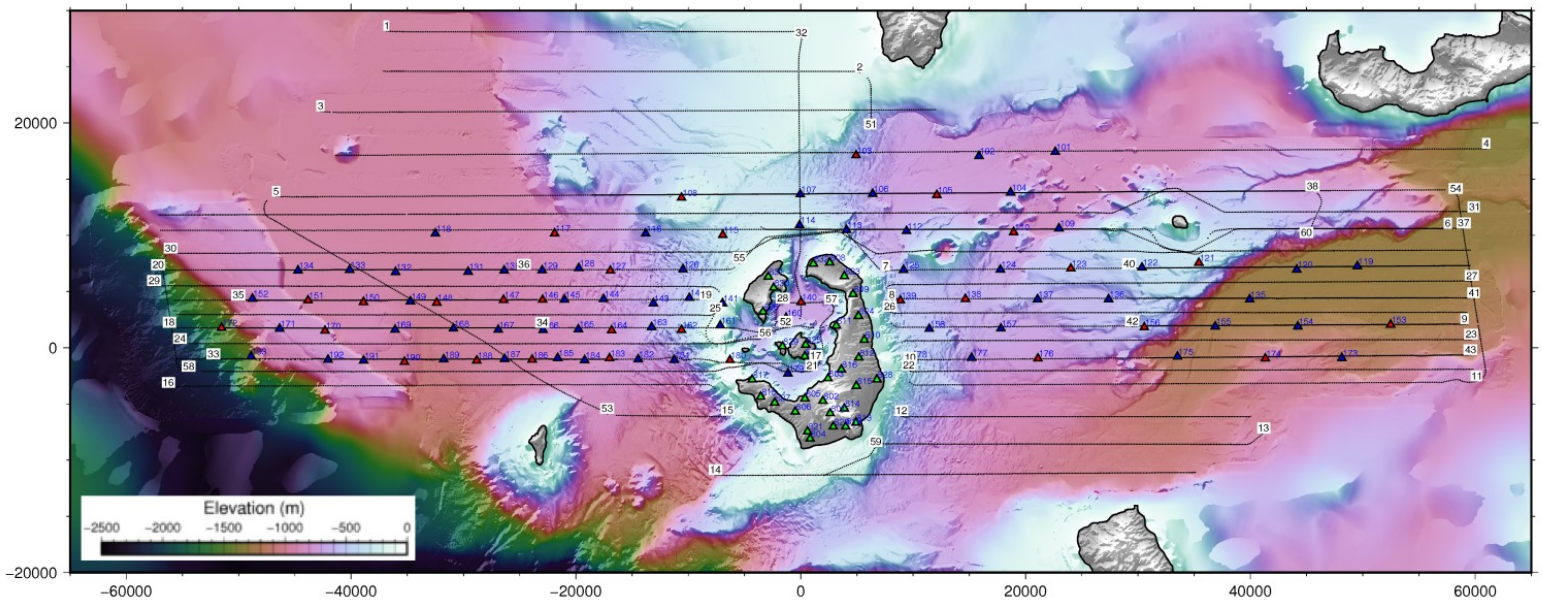

Travel-tomography results (Heath et al. 2019)

Results of high-quality travel-time tomography (Heath et al. 2019, Hooft et al. 2019, McVey et al. 2020) served as a starting model for this full-waveform inversion study.

Figure caption: "Velocity anomalies relative to the 1-D average velocity-depth profile at 1 km depth" (Heath et al. 2019)

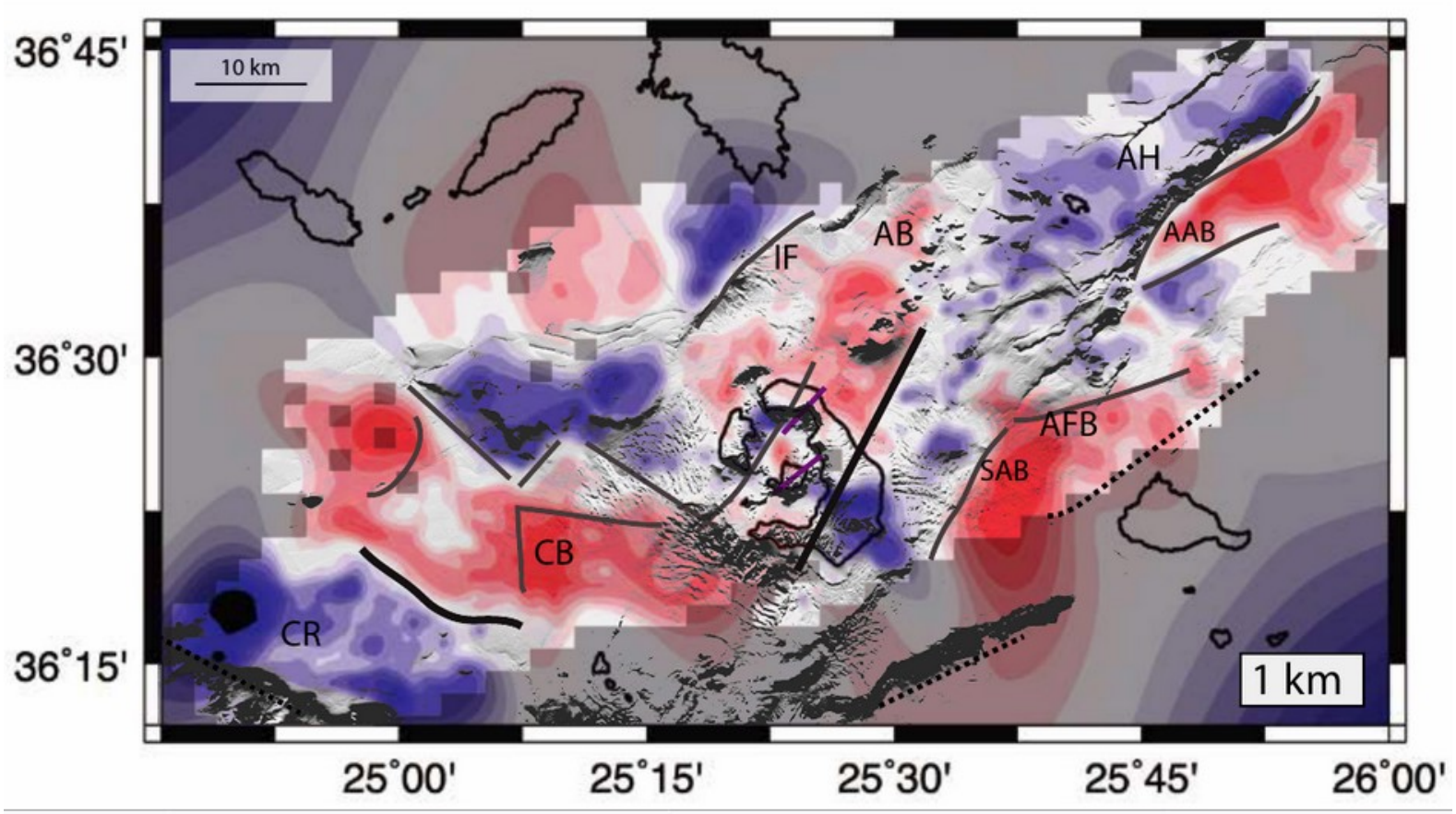

Full-waveform inversion

We use finite-difference `Fullwave3D` code (Warner et al. 2013) that has proved successful for oil&gas and other academic datasets.

Some of the parameters relevant to the inversion results shown here include: acoustic, isotropic wave equation with no attenuation; grid cell size 50 m in all directions; 50-grid-node-thick absorbing boundaries surrounding the model except for the top free-surface boundary; data-type: pressure (ocean-bottom hydrophones); data sampling 0.0025 s; trace length 5 s, data band-pass filtering (~2.5-5.5 Hz) and muting around early arrivals (window length 1 s) prior to the inversion; excluding data with offsets < 5 km; inverting mostly 'kinematics' of early arrivals (little attention to amplitudes or reflections); preconditioning of the gradient with approximate Hessian; inverting for slowness; ; smoothing of the model update: 2 local wavelengths horizontally, 1 local wavelength vertically; 4 subsequent iteration blocks with:

- 20 iterations at high-cut frequency 3.0 Hz
- 20 iterations at high-cut frequency 3.5 Hz
- 20 iterations at high-cut frequency 4.0 Hz
- 20 iterations at high-cut frequency 4.5 Hz.

Study area

indicated by the red rectangle. Axes are labeled with local coordinates in metres.

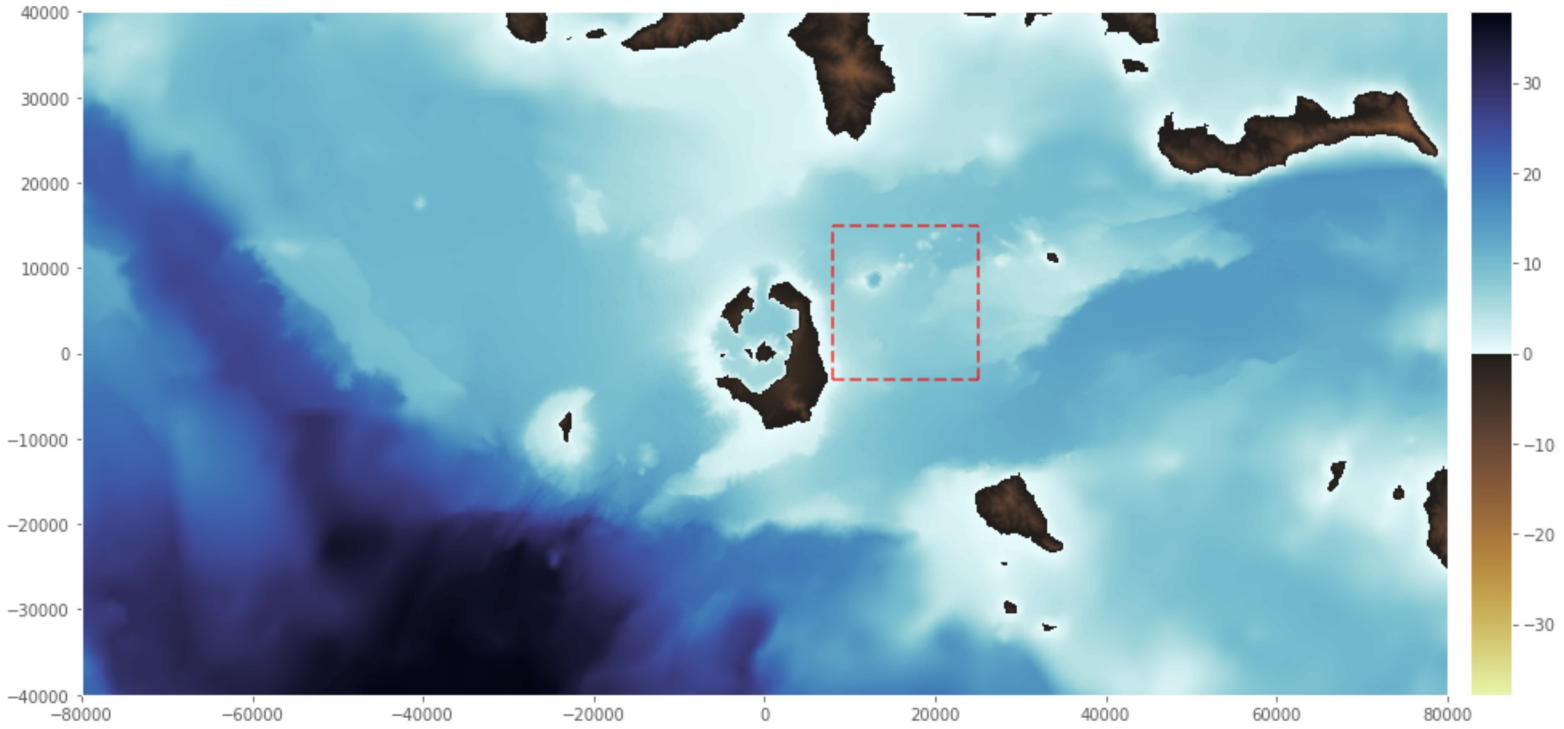

Shots and receivers

(grey and red dots respectively) projected onto a horizontal plane; X and Y axes in model grid nodes; receivers are annotated by their IDs; these IDs are referred to in other figures below; line 5 shown on other slides passes through stations 4105 and 4104.

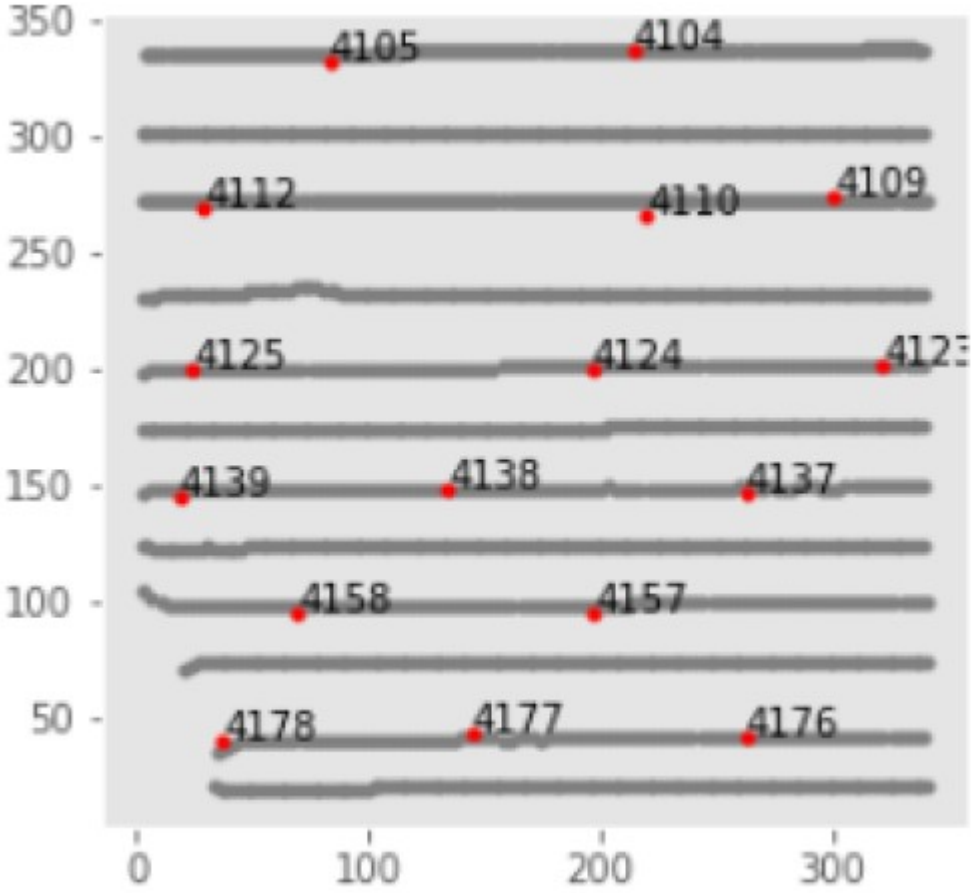

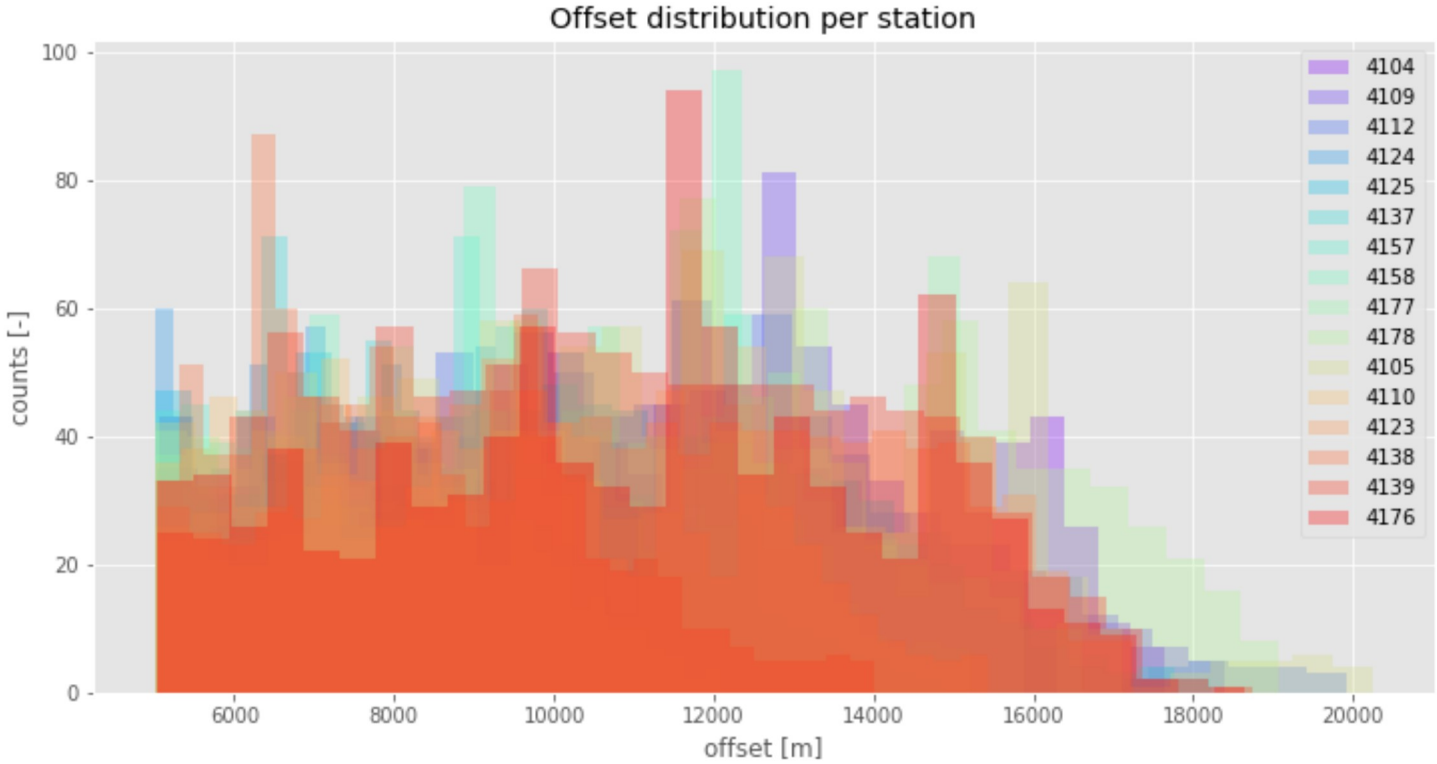
Offset distribution per station
counts [-]
offset [m]
0
20
40
60
80
100
6000
8000
10000
12000
14000
16000
18000
20000
4104
4109
4112
4124
4125
4137
4157
4158
4177
4178
4105
4110
4123
4138
4139
4176

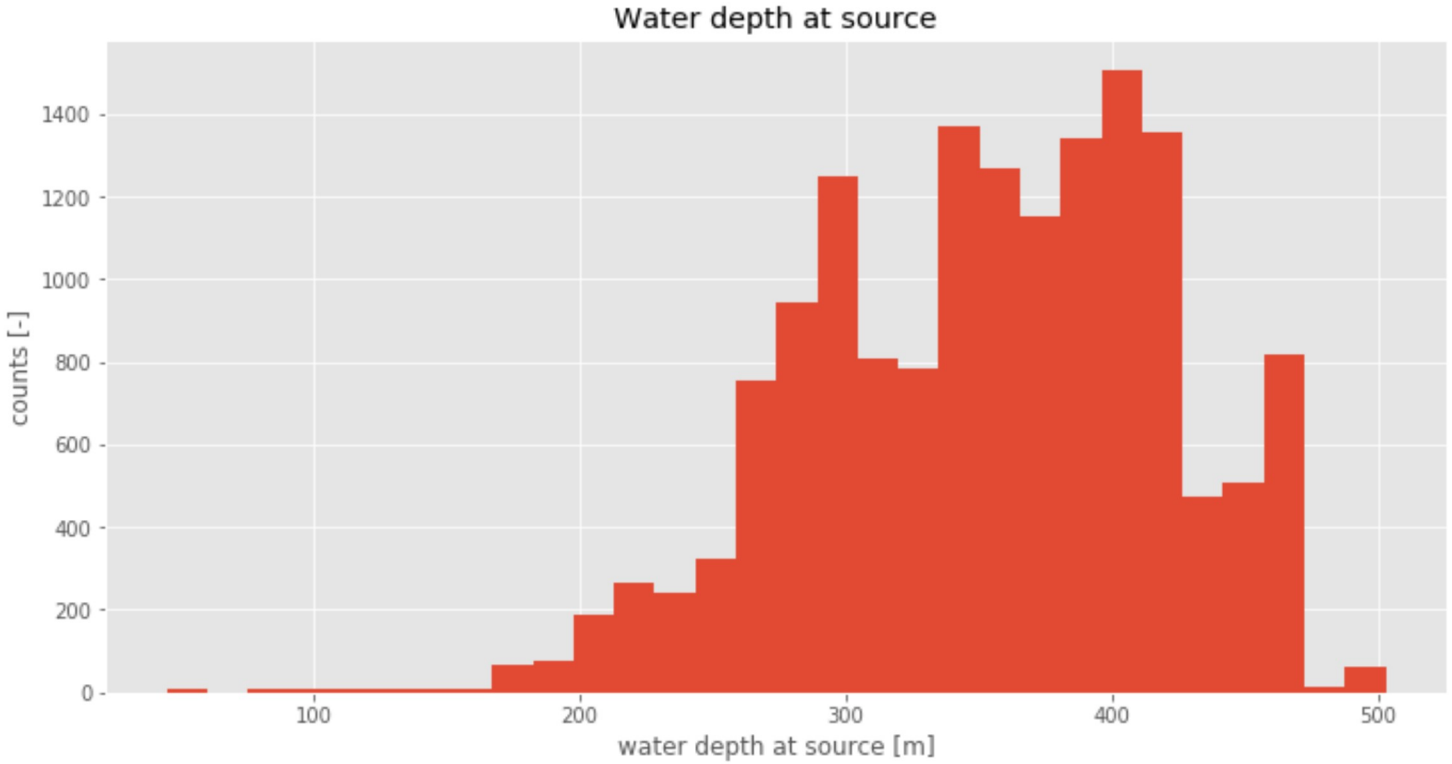
Water depth at source
counts [-]
0
200
400
600
800
1000
1200
1400
100
200
300
400
500
water depth at source [m]

Cost function evolution

each line represents one source; we use simple L2-norm cost function.

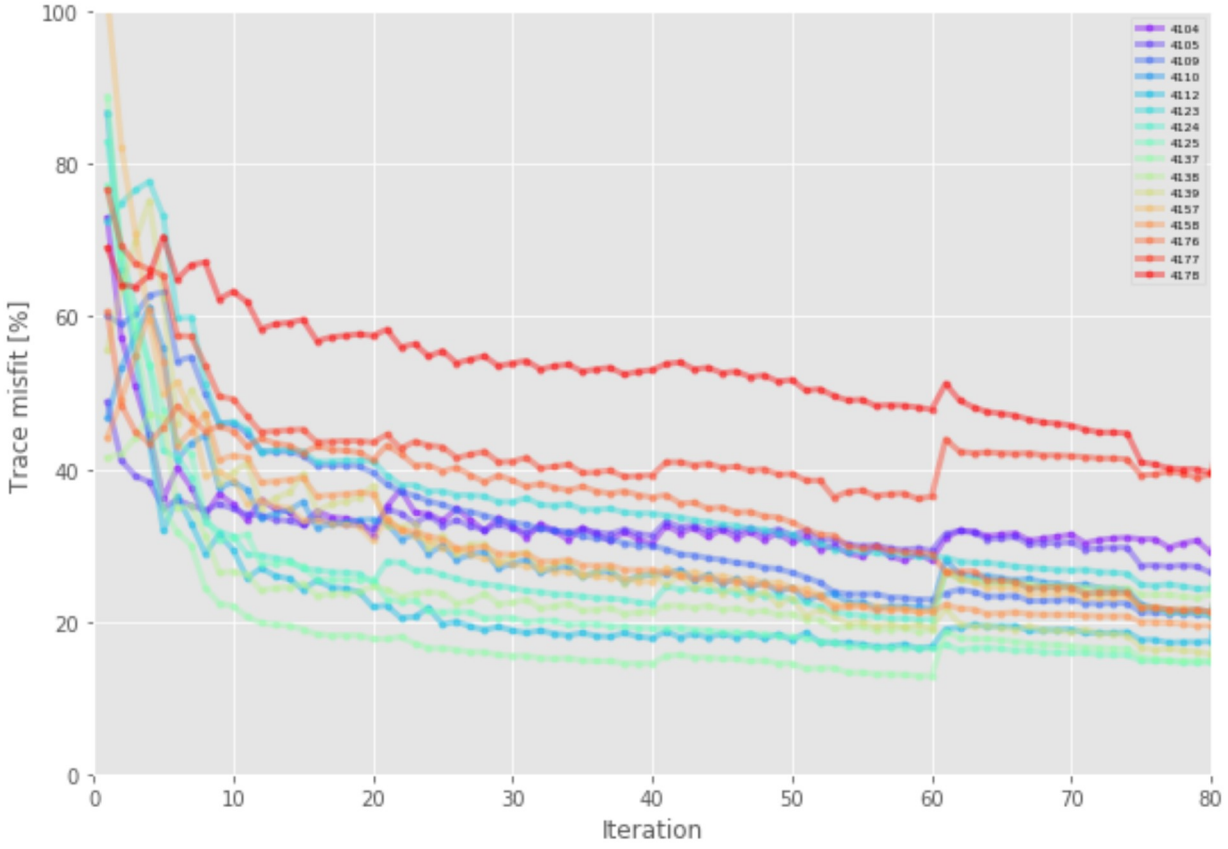

Traces fit, iteration 0

traces fit in time (left figure) and frequency (right figure) domain for station 4137, line 5; each figure consists of interlaced blocks of synthetic and observed traces; each block has 10 traces; first block in each figure corresponds to synthetic traces, second to observed, third to synthetic and so on; horizontal axis is labeled with trace numbers, vertical axis is labeled with time samples; data is normalized trace-wise to maximum value equal to 1 in both figures.

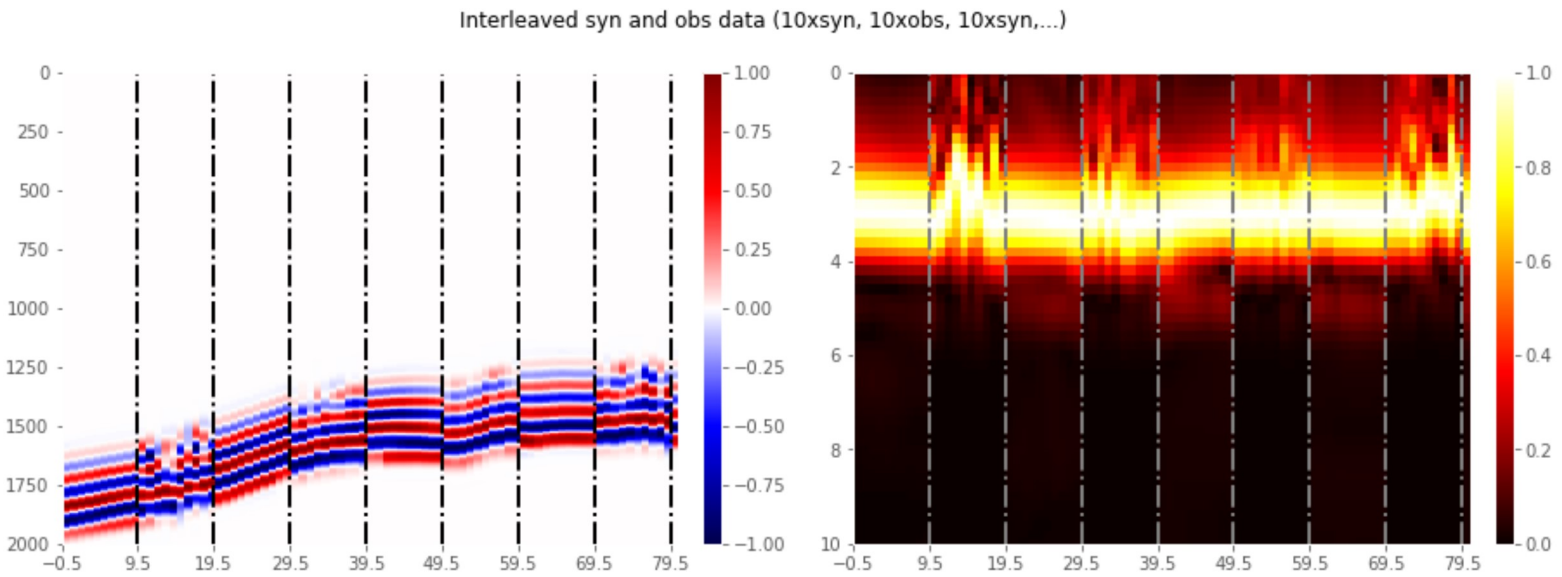

Traces fit, iteration 80

traces fit in time (left figure) and frequency (right figure) domain for station 4137, line 5; each figure consists of interlaced blocks of synthetic and observed traces; each block has 10 traces; first block in each figure corresponds to synthetic traces, second to observed, third to synthetic and so on; horizontal axis is labeled with trace numbers, vertical axis is labeled with time samples; data is normalized trace-wise to maximum value equal to 1 in both figures.

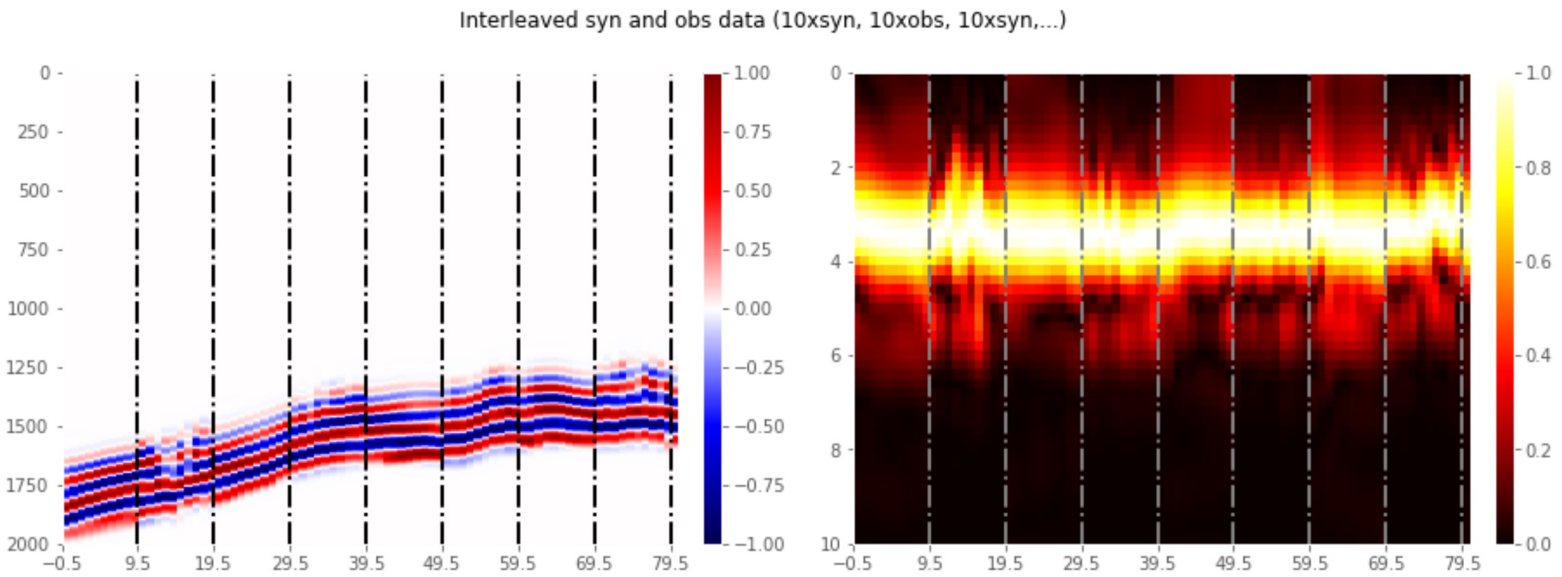

Phase comparison, iteration 0

the white star denotes station 4137; every colorful dot corresponds to a single receiver used in the inversion; color value denotes a phase (at 3 Hz) of data windowed in time around early arrivals. The left figure shows phase of the synthetic data, middle of the observed data and right is their difference wrapped into (-π,π) range. Color range varies from -π (blue) to π (red). Method based on Shah et al. 2012, Warner at al. 2013.

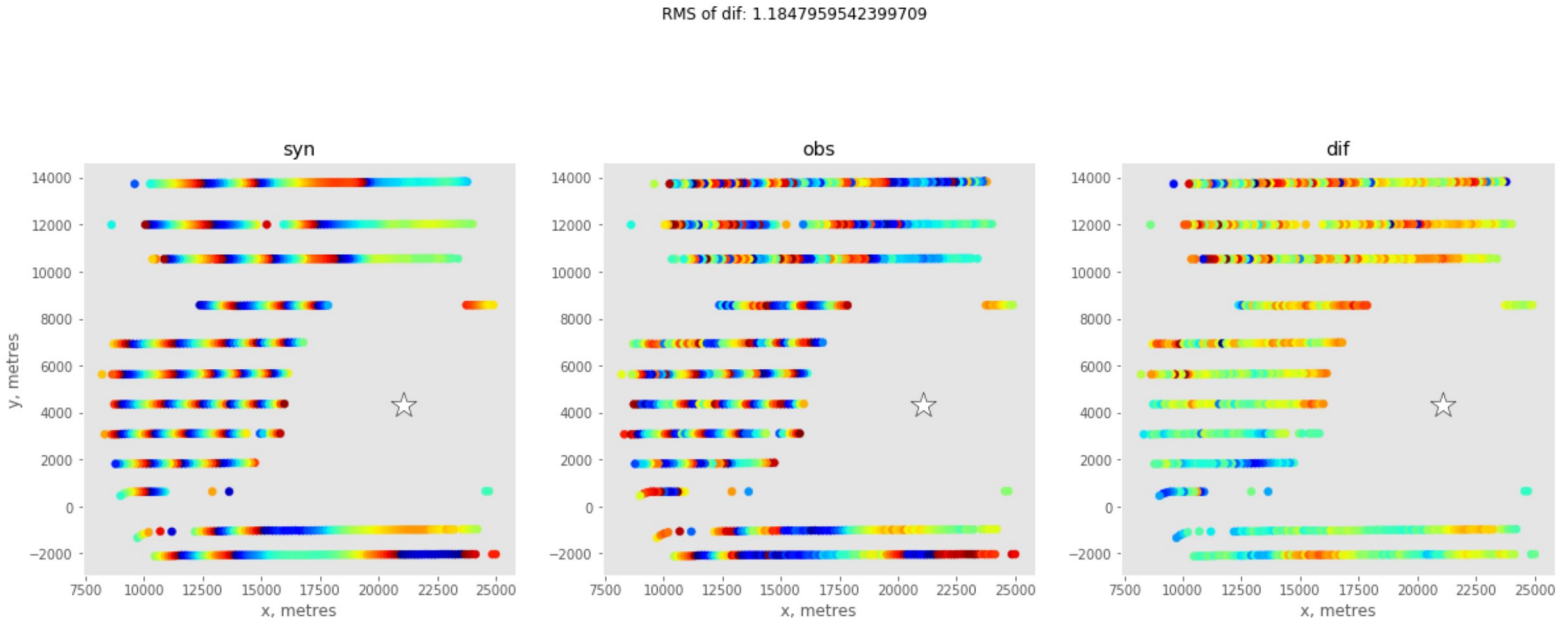

Phase comparison, iteration 80

the white star denotes station 4137; every colorful dot corresponds to a single receiver used in the inversion; color value denotes a phase (at 3 Hz) of data windowed in time around early arrivals. The left figure shows phase of the synthetic data, middle of the observed data and right is their difference wrapped into (-π,π) range. Color range varies from -π (blue) to π (red). Method based on Shah et al. 2012, Warner at al. 2013.

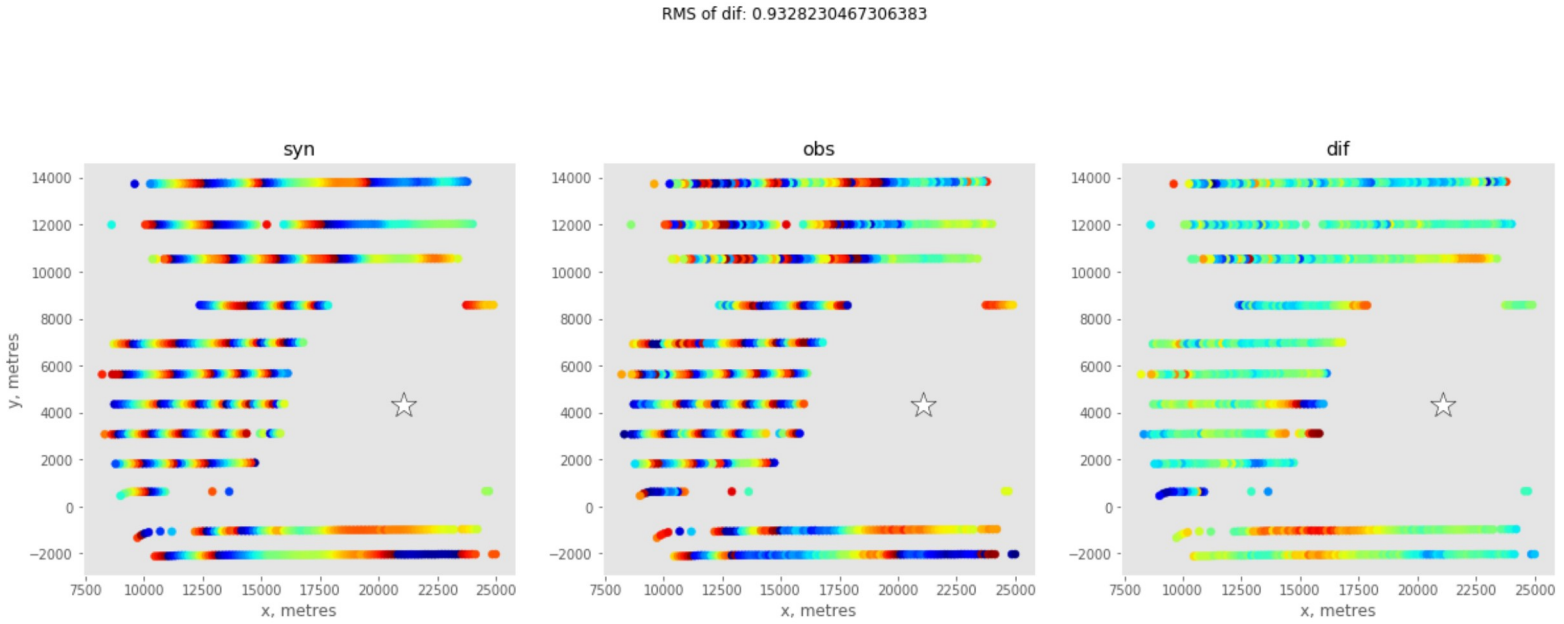

Phase-difference distribution

station 4137

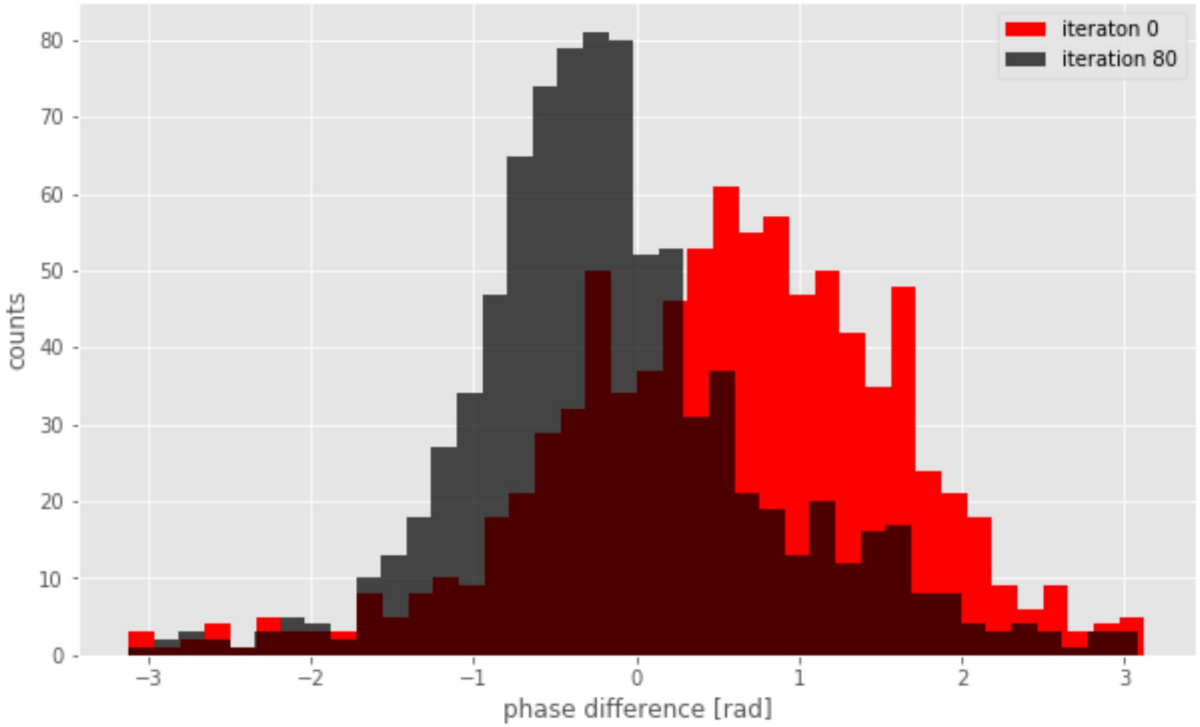

Vp model, iteration 0

white dashed lines are the cross-section lines; top left - xslice, top right - depth slice, bottom - yslice; all axes are labeled with model grid nodes; axes aspect ratios are different from 1:1.

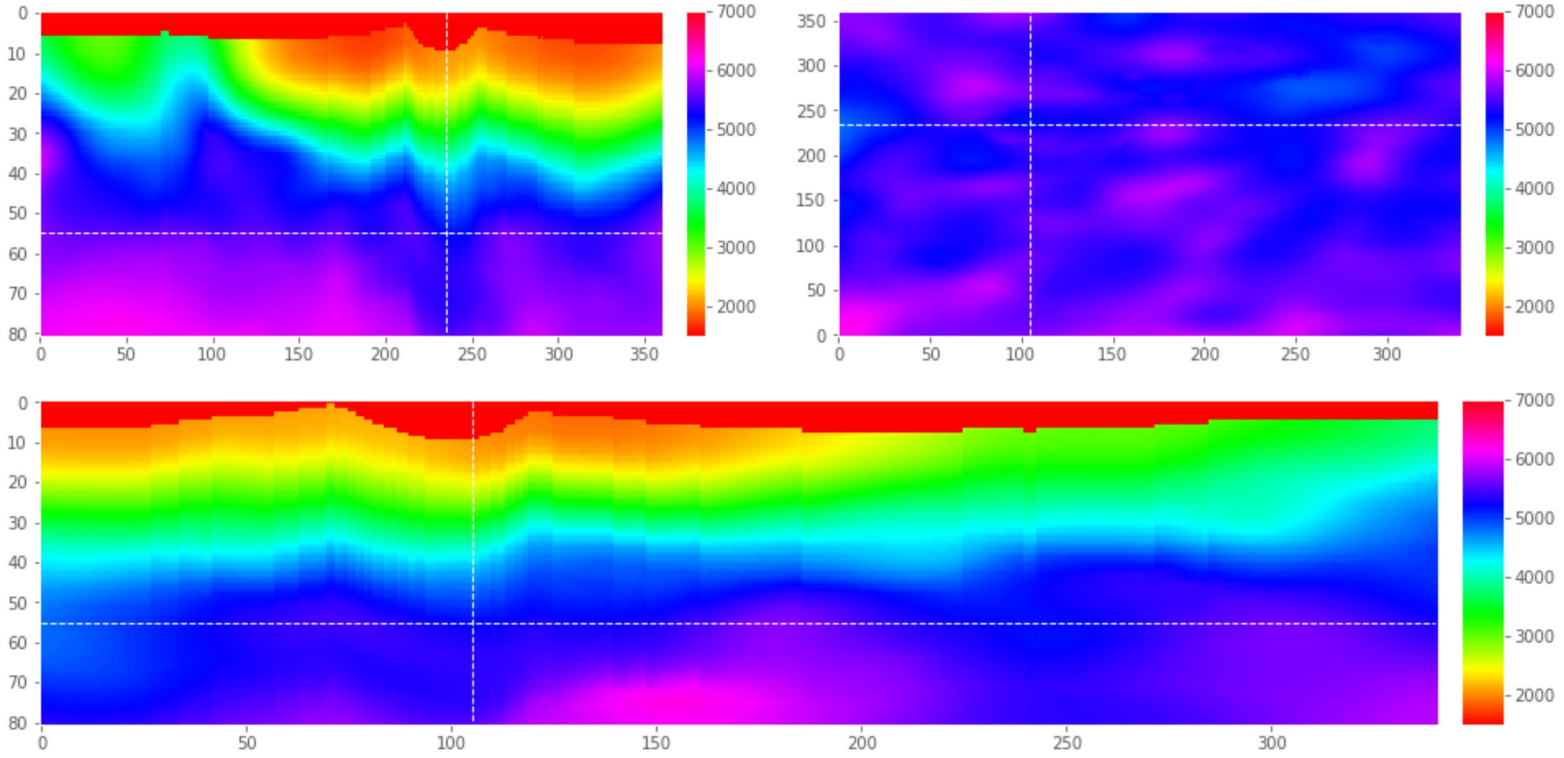

Vp model, iteration 5

white dashed lines are the cross-section lines; top left - xslice, top right - depth slice, bottom - yslice; all axes are labeled with model grid nodes; axes aspect ratios are different from 1:1.

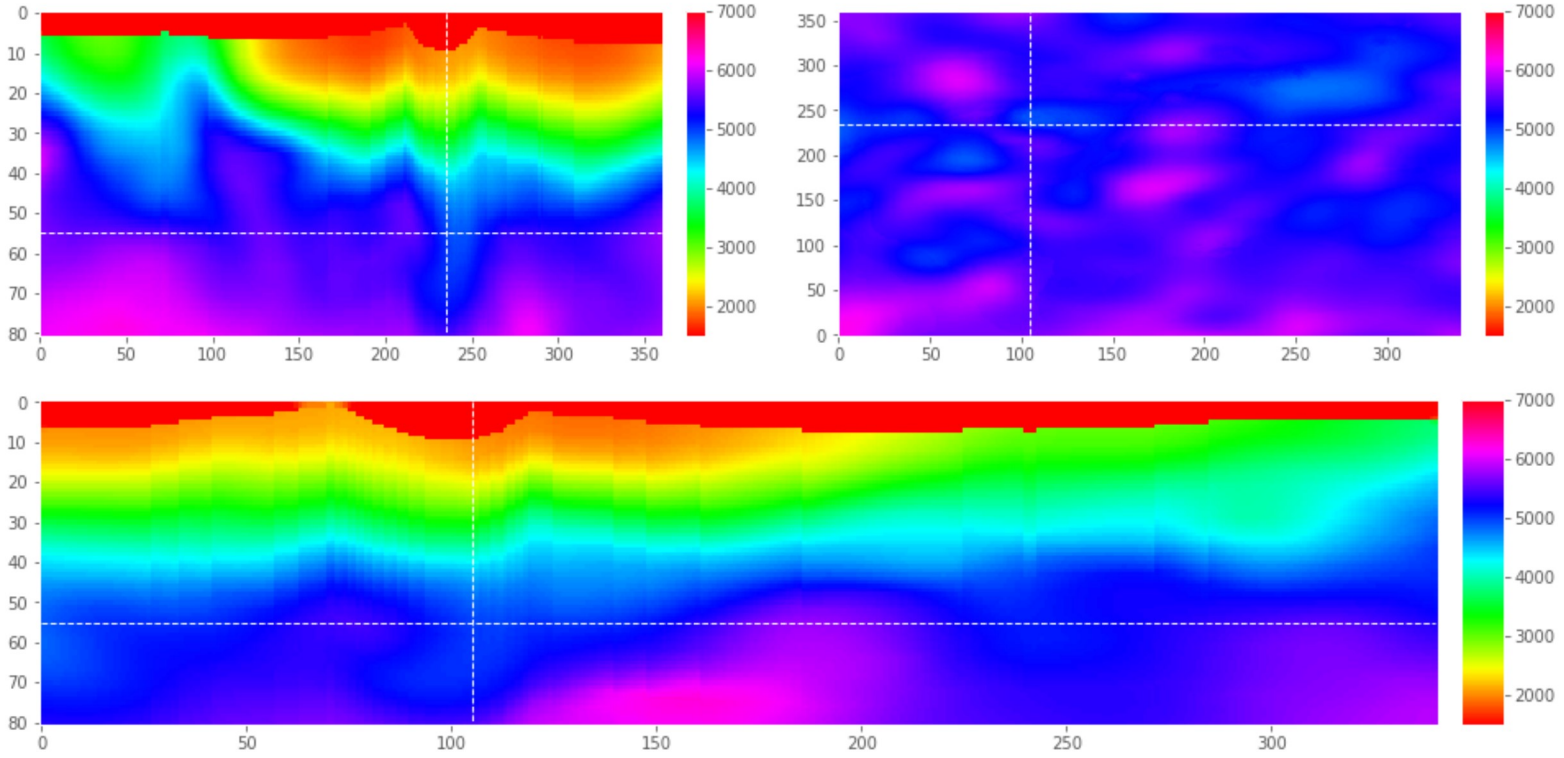

Vp model, iteration 10

white dashed lines are the cross-section lines; top left - xslice, top right - depth slice, bottom - yslice; all axes are labeled with model grid nodes; axes aspect ratios are different from 1:1.

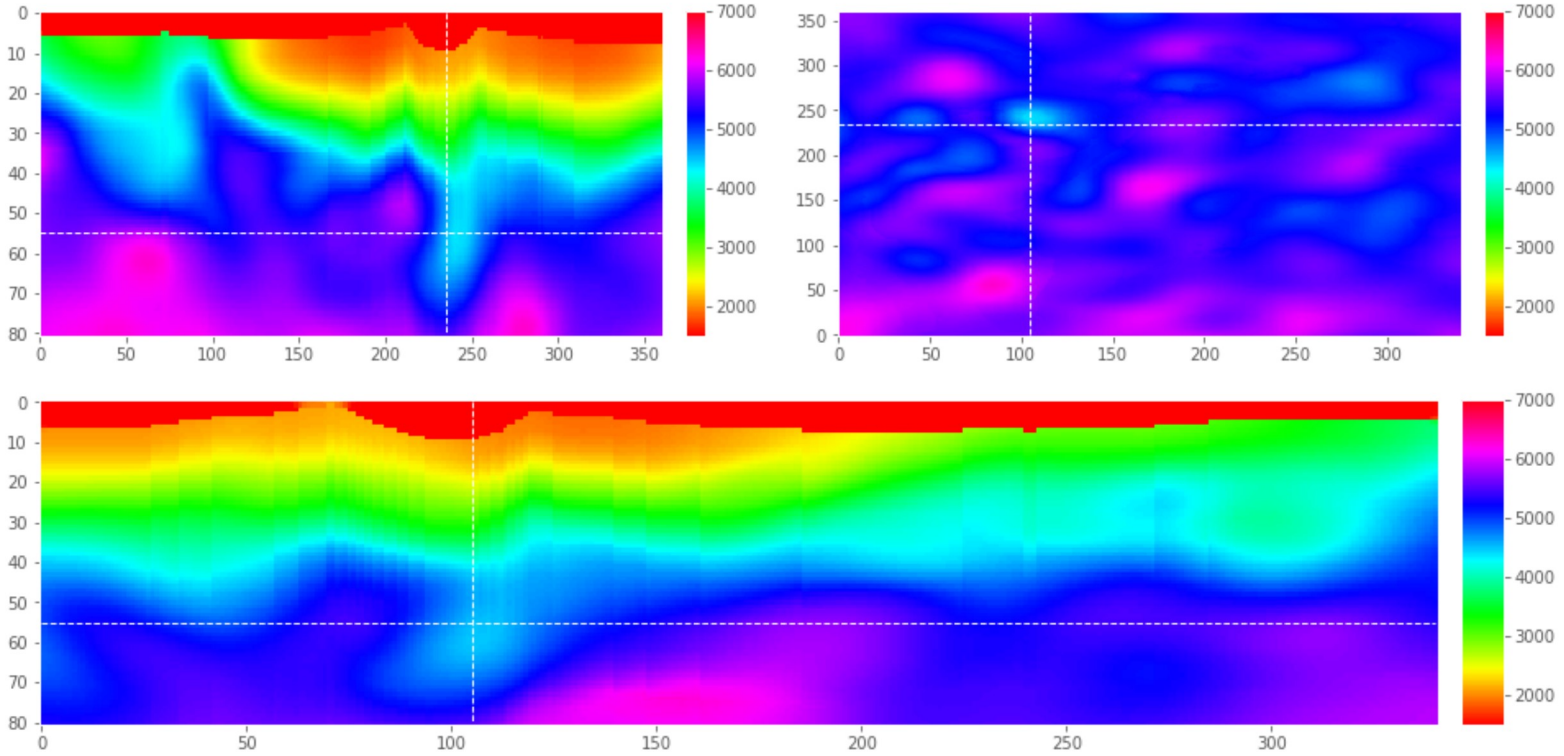

Vp model, iteration 20

white dashed lines are the cross-section lines; top left - xslice, top right - depth slice, bottom - yslice; all axes are labeled with model grid nodes; axes aspect ratios are different from 1:1.

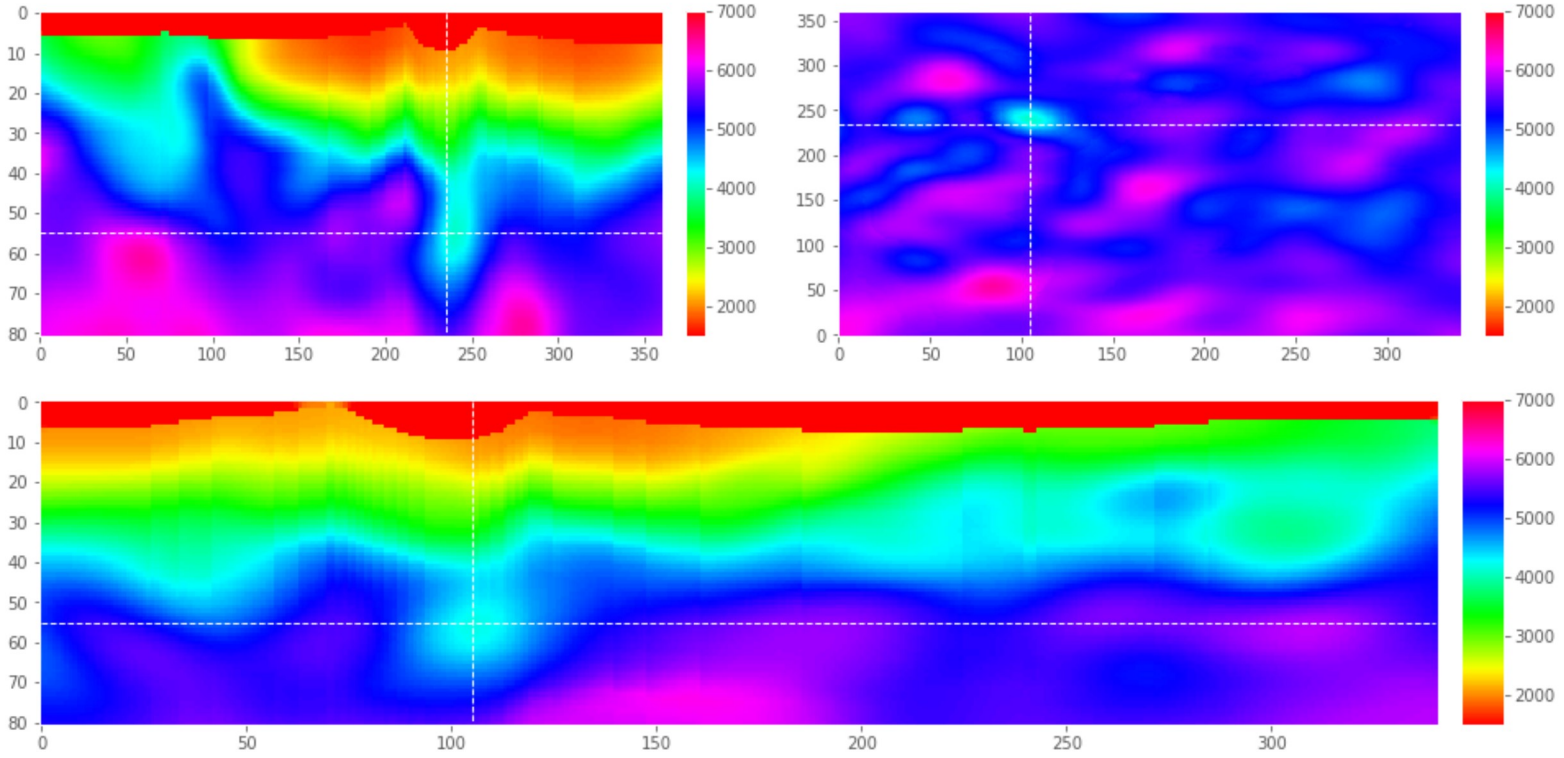

Vp model, iteration 40

white dashed lines are the cross-section lines; top left - xslice, top right - depth slice, bottom - yslice; all axes are labeled with model grid nodes; axes aspect ratios are different from 1:1.

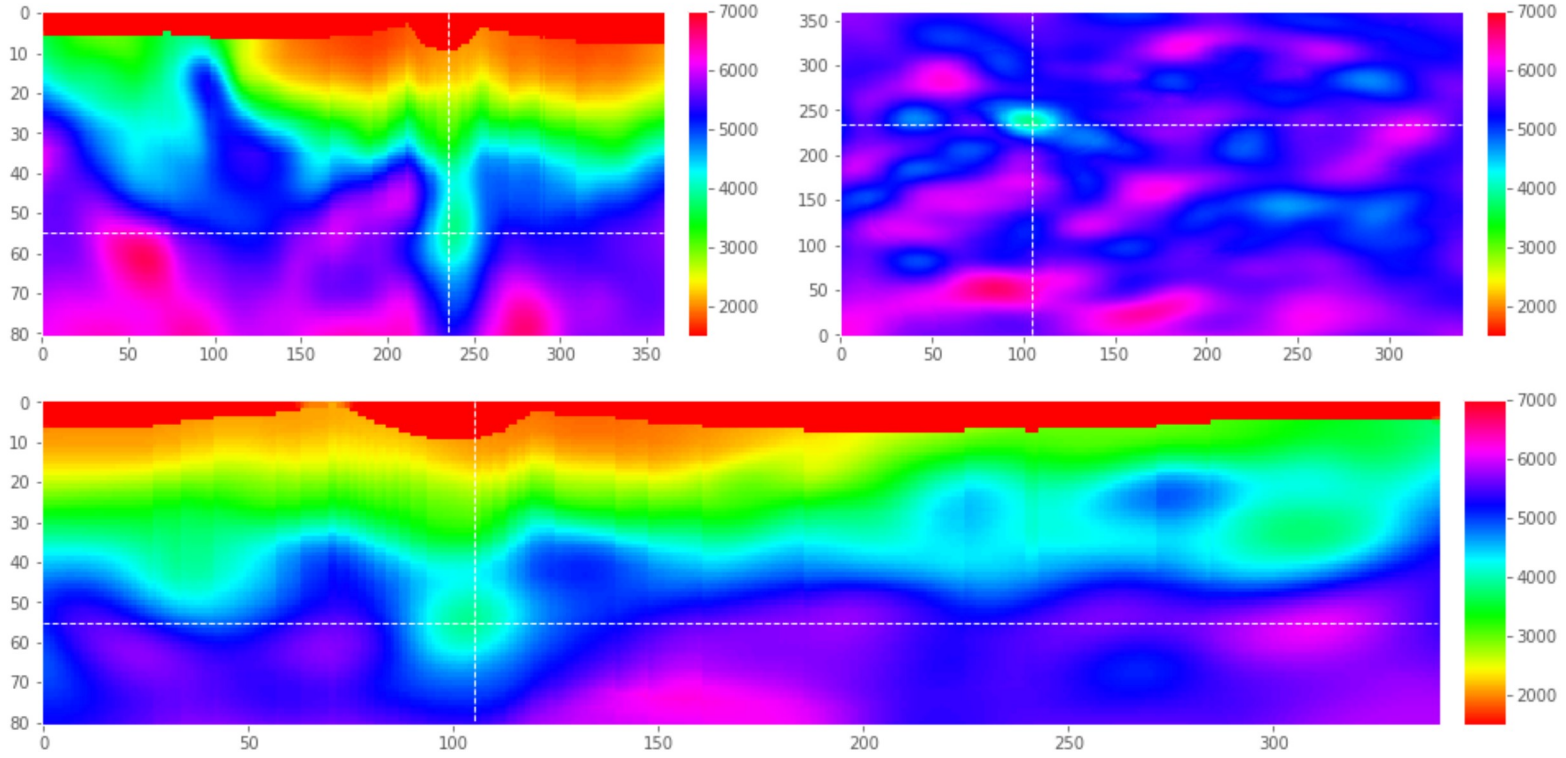

Vp model, iteration 80

white dashed lines are the cross-section lines; top left - xslice, top right - depth slice, bottom - yslice; all axes are labeled with model grid nodes; axes aspect ratios are different from 1:1.

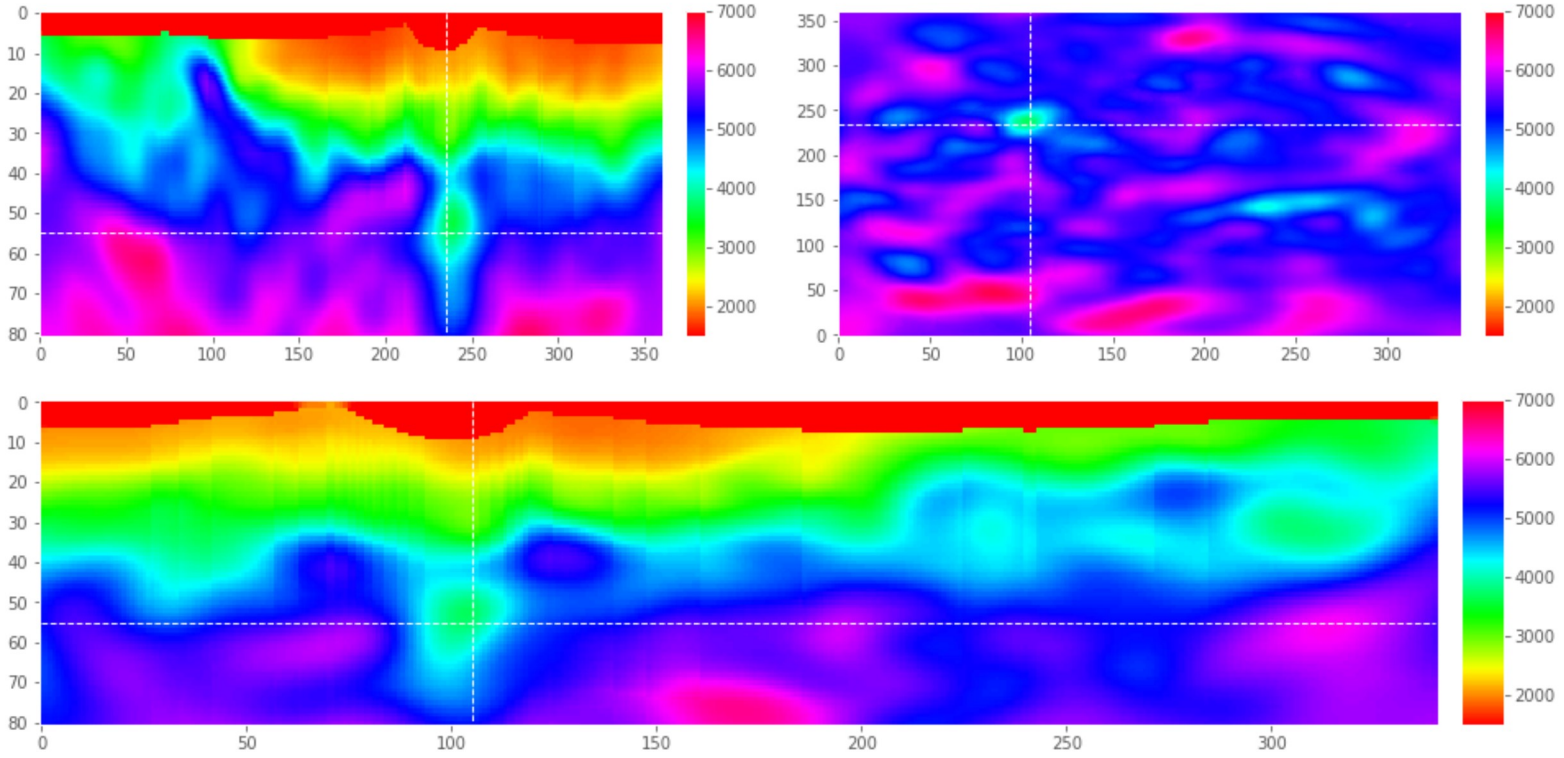

Pressure-to-particle-velocity conversion

We implemented a method to jointly invert pressure and vertical particle-velocity data using reciprocity. Figure below demonstrates its correctness. Meaning of different columns (panels) is the same as in the previous phase-plots, and so is the acquisition geometry (except that here all the traces are included, regardless of the quality and offset) and frequency. Each row demonstrates different scenario. Top row compares pressure synthetic and pressure observed data, RMS of the differences is 1.52. Middle row compares pressure synthetic and vertical particle-velocity data. RMS is much higher, 2.06 which indicates inadequacy of the simulated data. Finally, bottom row shows vertical particle-velocity synthetic and observed data, RMS is similar to the first case: 1.57.

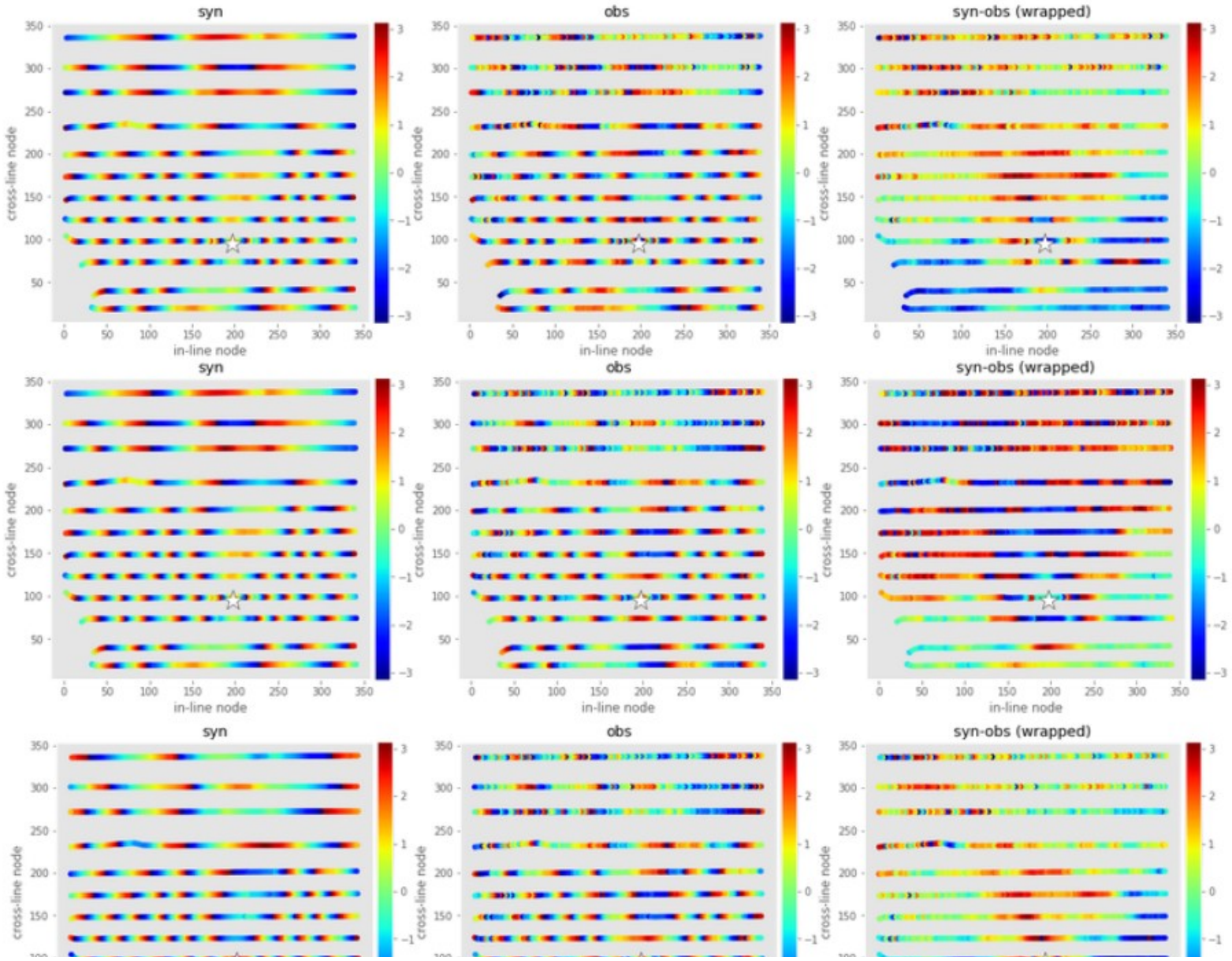
syn
obs
syn-obs (wrapped)
cross-line node
in-line node

Inversion in Christiana sedimentary basin

Below we show a vertical 'in-line' slice of the starting and final (after 80 iterations) model of a ~40-km long portion of the Christiana basin on the W side of the Santorini caldera. The model depth is 5 km. We include the cost function evolution plot analogous to that of Kolumbo.

```
plt.figure(figsize=(32,4))
i04.o.vp.it[0].plot(cmap='hsv')
plt.gca().set_aspect('equal')
```

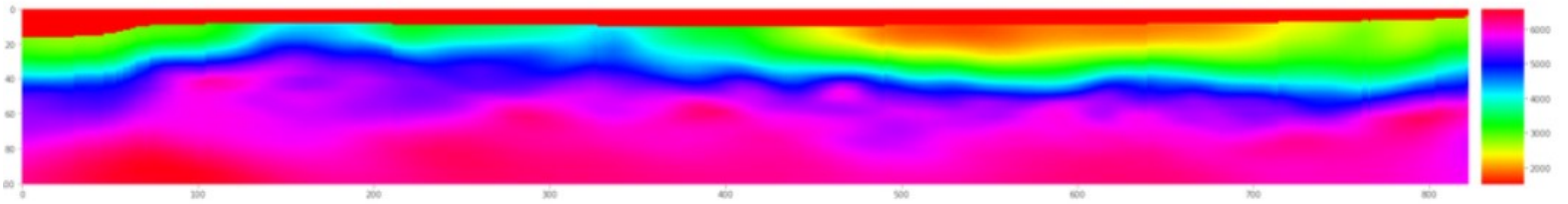

```
plt.figure(figsize=(32,4))
i04.o.vp.it[80].plot(cmap='hsv')
plt.gca().set_aspect('equal')
```

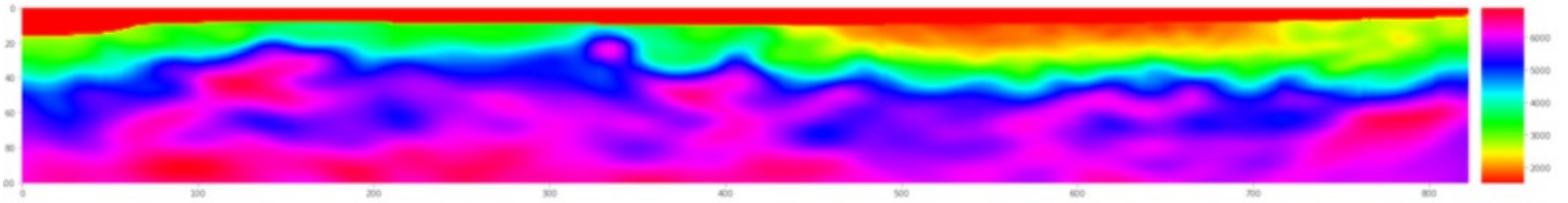

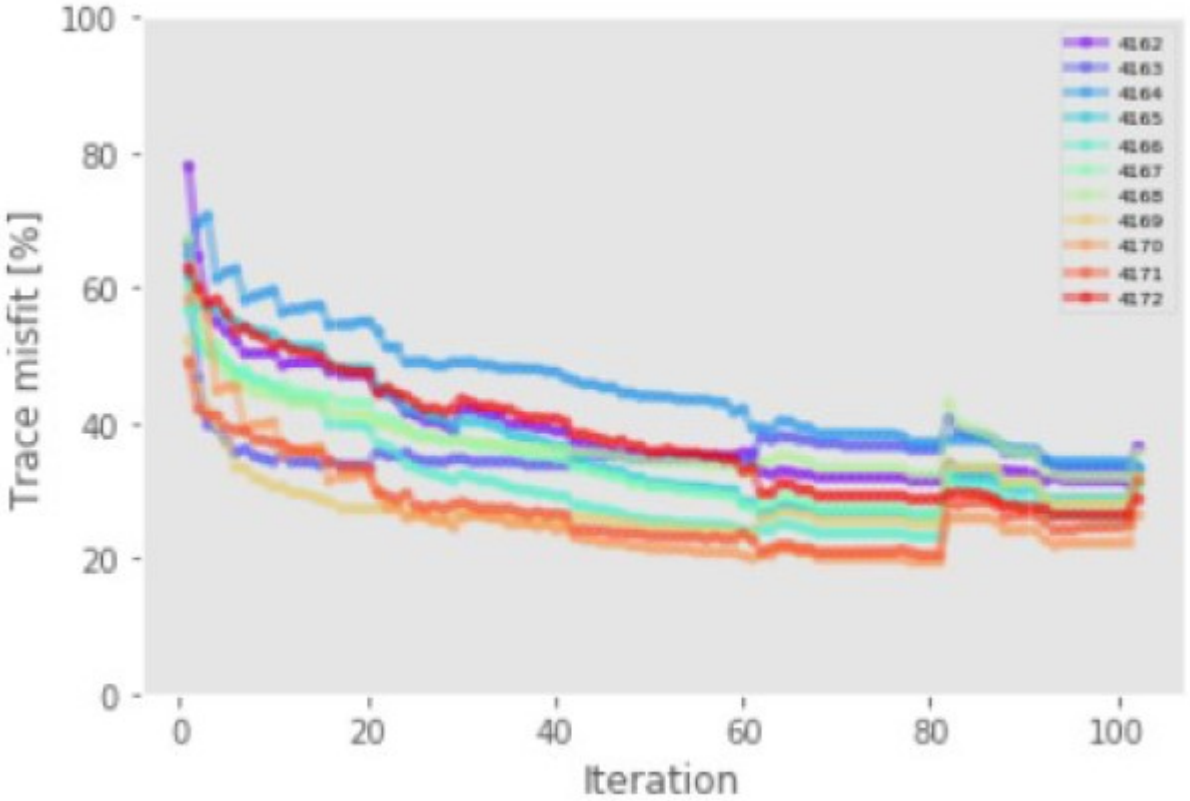
100
80
60
40
20
0
Trace misfit [%]
0
20
40
60
80
100
Iteration
4162
4163
4164
4165
4166
4167
4168
4169
4170
4171
4172

Towards all-data inversion

We implemented the immersed-boundary method to simulate waves reflecting from the steep caldera walls (see the first of the figures below, the pressure wavefield at one node below the free surface is shown). The code has already been used in the industry. We used it to invert the OBS data around the caldera. Inversion of the OBS data alone is compromised by the sparsity of the stations inside the caldera (see the second figure displaying the lines connecting every source and receiver). The results are nonetheless promising though still preliminary. Thus they are not shown here. We also implemented a method to inject the the energy at the rugged free surface to correctly simulate recordings of our land stations. Forward calculations and synthetic vs. observed data comparisons proves the method is correct.

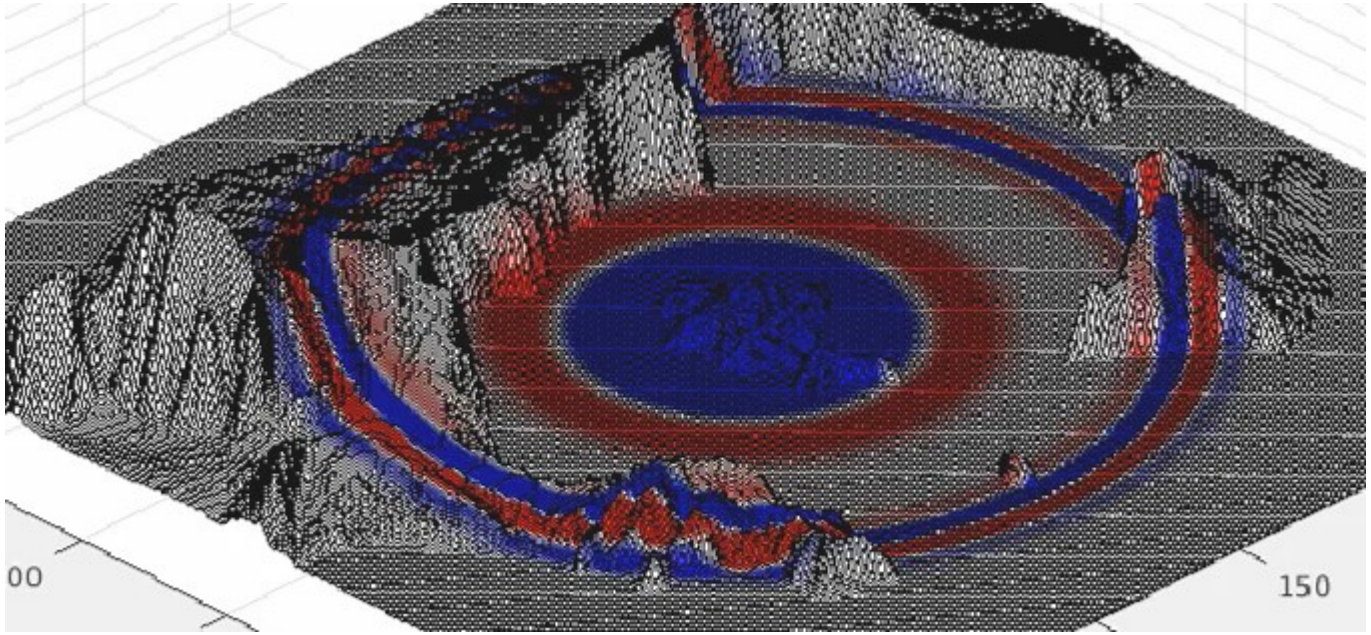

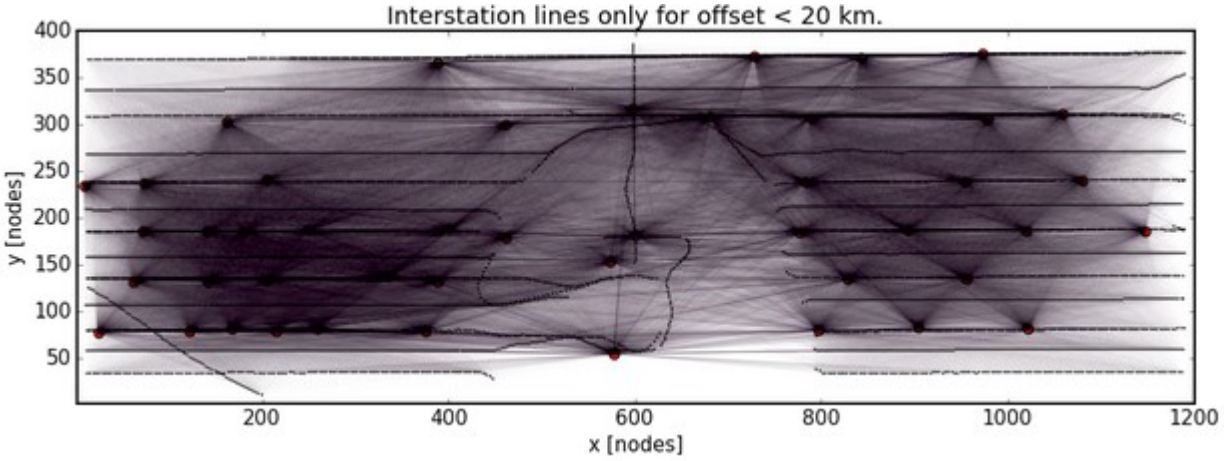
Interstation lines only for offset < 20 km.
400
350
300
250
200
150
100
50
y [nodes]
200
400
600
800
1000
1200
x [nodes]

Summary

- we detect a distinct low-velocity zone under the Kolumbo cone overlooked by travel-tomography most likely due to its limited spatial extent
- the feature is robust, we have run multiple inversions with different parameters (varying smoothing, no. of iterations, frequencies etc.), also using particle-velocity (vertical component) data, and different starting model (obtained using slightly different set of first-break picks)
- we plan to investigate it further using more data and anisotropic wave equation with attenuation
- we have also run inversions in the sedimentary basin on the other side of Santorini caldera that prove that our method gives physically plausible results
- we implemented immersed-boundary method of simulating irregular free surface within the finite-difference scheme; the approach includes careful injection of the energy at the free surface to simulate land-station data using reciprocity principle.

References

- Heath, B. A., E. E.E. Hooft, D. R. Toomey, C. B. Papazachos, P. Nomikou, M. Paulatto, J. V. Morgan, and M. R. Warner. 2019. “Tectonism and Its Relation to Magmatism Around Santorini Volcano From Upper Crustal P Wave Velocity.” Journal of Geophysical Research: Solid Earth 124: 10610–29.
- Hooft, E E E, B A Heath, D R Toomey, M Paulatto, C B Papazachos, P Nomikou, J V Morgan, and M Warner. 2019. “Seismic Imaging of Santorini: Subsurface Constraints on Caldera Collapse and Present-Day Magma Recharge.” Earth and Planetary Science Letters 514: 48–61.
- Hooft, Emilie E.E., Paraskevi Nomikou, Douglas R. Toomey, Danai Lampridou, Claire Getz, Maria-Eleni Christopoulou, Daniel O’Hara, et al. 2017. “Backarc Tectonism, Volcanism, and Mass Wasting Shape Seafloor Morphology in the Santorini-Christiana-Amorgos Region of the Hellenic Volcanic Arc.” Tectonophysics 712: 396–414.
- Kilias, Stephanos P., Paraskevi Nomikou, Dimitrios Papanikolaou, Paraskevi N. Polymenakou, Athanasios Godelitsas, Ariadne Argyraki, Steven Carey, et al. 2013. “New Insights into Hydrothermal Vent Processes in the Unique Shallow-Submarine Arc-Volcano, Kolumbo (Santorini), Greece.” Scientific Reports 3: 1–13.
- McVey, Brennah Gene, Emilie E.E. Hooft, Benjamin A. Heath, Douglas R. Toomey, Michele Paulatto, Joanna V. Morgan, Paraskevi Nomikou, and Constantinos B. Papazachos. 2020. “Magma Accumulation beneath Santorini Volcano from P-Wave Tomography.” Geology 48.
- Shah, Nikhil, Mike Warner, Tenice Nangoo, Adrian Umpleby, Ivan Stekl, Jo Morgan, and Lluis Guasch. 2012. “Quality Assured Full-Waveform Inversion : Ensuring Starting Model Adequacy.” In SEG Technical Program Expanded Abstracts 2012, 1–5.
- Warner, Michael, Andrew Ratcliffe, Tenice Nangoo, Joanna Morgan, Adrian Umpleby, Nikhil Shah, Vetle Vinje, et al. 2013. “Anisotropic 3D Full-Waveform Inversion.” Geophysics 78: R59–80.